Visualization of Shape Motions in Shape Space

Vahid Taimouri and Jing Hua, *Member, IEEE*

Abstract—Analysis of dynamic object deformations such as cardiac motion is of great importance, especially when there is a necessity to visualize and compare the deformation behavior across subjects. However, there is a lack of effective techniques for comparative visualization and assessment of a collection of motion data due to its 4-dimensional nature, i.e., timely varying three-dimensional shapes. From the geometric point of view, the motion change can be considered as a function defined on the 2D manifold of the surface. This paper presents a novel classification and visualization method based on a medial surface shape space, in which two novel shape descriptors are defined, for discriminating normal and abnormal human heart deformations as well as localizing the abnormal motion regions. In our medial surface shape space, the geodesic distance connecting two points in the space measures the similarity between their corresponding medial surfaces, which can quantify the similarity and disparity of the 3D heart motions. Furthermore, the novel descriptors can effectively localize the inconsistently deforming myopathic regions on the left ventricle. An easy visualization of heart motion sequences on the projected space allows users to distinguish the deformation differences. Our experimental results on both synthetic and real imaging data show that this method can automatically classify the healthy and myopathic subjects and accurately detect myopathic regions on the left ventricle, which outperforms other conventional cardiac diagnostic methods.

Index Terms—Medial surface, shape space, comparative visualization, left ventricle diagnosis

1 Introduction

Generally, analysis of dynamic three-dimensional object deformations such as cardiac motion, face expressions, and gestures is of great importance, especially when there is a necessity to visualize and compare the deformation behavior across subjects. Physical based approaches such as deformable models assume the deformation is governed by some physical principles, and estimate the deformation by minimizing an appropriate energy functional subject to deformation smoothness, which is achieved through finite element analysis. In geometric based approaches, a higher level of shape abstraction and information reduction is necessary to support efficient characterization of shape motions. In machine vision techniques, a shape descriptor extracts local/global geometric features from the shape [41, 8, 42], and then, an energy functional based on the shape descriptor is minimized to classify the shapes. The modern geometry introduces shape space, where coordinates of points in the space represent some generalized properties related to various geometrical structures [4, 5].

In information visualization, the motion typology was used to achieve a perceptual grouping effect on information analysis [3], in which the users are more concern about how the data evolves. However, due to the large amount of spatial and temporal data, it is difficult for the human to perceive and interact with the information [37]. Elmqvist *et al.* proposed a technique, called Growing Polygons, which provides a graphical representation such as colors, textures, and animation, for better understanding of the information flow [11]. Ji *et al.* [18] combined the static and dynamic view selection methods so that the user can perceive the maximum amount of information from time-varying data. Moere [26] employed the information flocking concept to generate dynamic patterns in time-varying data based upon long-term as well as short-term temporal similarities. In this work, we analyze the shape variability of dynamic objects by encoding and compressing them in shape space. In other words, each group of shapes relates to the points in the shape space manifold, which is used to model the shape variability. The shape variability analysis can be used to capture the deformation of the dynamic objects and lower complexity of analyzing the deformations in a high dimensional Euclidean space.

One major area where the dynamic shape analysis and visualization can be immensely helpful is medical imaging analysis. Analysis of dynamic organs, such as cardiac motion, always requires high expertise in order to achieve accurate early clinical diagnosis. This paper aims at classification of normal and abnormal left ventricle (LV) deformations by statistical analysis of the LV variability in shape space. Cardiomyopathy is one of major cardiac disease, especially in children, which affects the myocardium such that the left ventricle cannot be filled as in a normal left ventricle [29]. The traditional cardiac diagnosis methods are mainly based on general global volumetric measures such as left ventricular volume, left ventricular mass, ejection fraction, and cardiac output. However, certain local shape descriptors such as strain analysis, mean and Gaussian curvature, shape index, shape spectrum, and wall thickness can provide much richer information for the cardiac analysis [15]. As cardiomyopathy affects the wall thickness of the left ventricle such that in the myopathic regions, the wall thickness changes less than the healthy regions, we can compare the wall motion and its thickness change to visualize, classify and localize the myopathic regions on the left ventricle.

In this paper, we embed a sequence of poses, i.e., shapes, of the left ventricle motion during one heart cycle as the points on the shape space manifold, and define the similarity between each pair of poses by measuring the geodesic distance between their corresponding points on the shape space manifold. Therefore, each deformation can be represented by a high-dimensional curve on the non-linear shape space manifold, and the deformation classification problem is converted to the high-dimensional curve classification problem.

1.1 Related Work

In many cardiac analysis approaches, Wall Thickness (WT) is used as a sensitive indicator of abnormal cardiac contraction and expansion [2]. WT is mainly computed by drawing line segments perpendicular to the centerline of the endocardial and epicardial contours at each slice [31]. As a 3D extension of this method, the *center-surface* model provides a viable framework to describe shape parameters such as WT and bending which do not belong to the linear Euclidean space [15, 7]. Therefore, the linear shape analysis techniques do not apply to these parameters. The medial surface of a 3D object consists of the centers of all spheres that are interior to the object and tangent to the object's boundary at two or more points.

- *Vahid Taimouri was with Department of Computer Science at Wayne State University when conducting this work, and is now with Department of Radiology at Children's Hospital Boston, Harvard Medical School, Boston, MA, 02115, USA. E-mail: vahid.taimouri@childrens.harvard.edu.*
- *Jing Hua is with Department of Computer Science, Wayne State University, Detroit, MI, 48202, USA. E-mail: jinghua@wayne.edu.*

Manuscript received 31 March 2013; accepted 1 August 2013; posted online 13 October 2013; mailed on 4 October 2013.
For information on obtaining reprints of this article, please send e-mail to: tvcg@computer.org.

Medial representation (m-Reps) [27, 10] and continuous medial representations (cm-Reps) [40, 39] are deformable parametric representations of the boundary-medial relationship, which are deformed to fit the interiors of objects to the model structure. Terriberry *et al.* presented a 3D medial surface based on subdivision surfaces, which is parameterized over a fixed domain and can support the complex medial surface with more than one medial surface [36]. Sun *et al.* applied the medial model to the right and left ventricle deformations and concluded that the medial model can capture the deformation of the left and right ventricles along with the changes of their wall thickness over time [33, 34].

Fletcher *et al.* [13] presented principal geodesic analysis (PGA) as a generalization of principal component analysis (PCA) to compute the variability of data on a manifold. The method considers the intrinsic properties of the manifold such as geodesic curves and distance for calculation of shape variability. They used Riemannian log map to project the points of the non-linear shape space manifold onto the linear tangent space, which is distance preserving map, whereas the orthogonal map is not [20, 21]. They tested PGA by computing the shape variability on a hippocampus data set. In addition, the points on the tangent space can be projected back to the shape space manifold using the Riemannian exponential map.

This paper aims to differentiate motions across subjects, in particular, the healthy and myopathic left ventricles based on the changes of the LV wall thickness. Towards this end, a non-linear shape space framework based on m-Reps is introduced, which can capture the characteristics of the LV deformation, using two new shape descriptors. Consequently, the log map can be employed to project the non-linear space onto a linear one and measure the similarity between different medial surface deformations. Our contributions in this paper can be summarized as follows,

- A new shape space based on the medial surface and thickness function is introduced, where the geodesic distance between two embedding points measures the similarity of the corresponding deforming shapes;
- Two novel shape descriptors are defined in the shape space, which can discriminate different deformations and detect their differences;
- The effectiveness of the medial surface shape space is demonstrated for visualization and classification of the left ventricle deformations.

The remainder of this paper is organized as follows. The shape space theoretical background is reviewed in Section 2; the medial surface shape space and the classification framework are introduced in Section 3; the experimental results on the synthetic and real left ventricle datasets are illustrated in Section 4 and Section 5, followed by Conclusions in Section 6.

2 Shape Space Theory

Let X be a topological space and $\sim$ be an equivalence relation. The equivalence class of y is defined as,

$$[y] = \{x \in X | y \sim x\}.$$

The set of all equivalence classes in X w.r.t. to $\sim$ is called *quotient space* of X by $\sim$, i.e. $X/\sim = \{[x] : x \in X\}$. Each equivalence class has a projection map π which maps each element of X to its equivalence class,

$$\pi : X \to X/\sim, [x] = \pi(x).$$

Assume a high dimensional space $\mathbf{N}$ in which each point characterizes one shape, e.g., the space all immersions of a fixed connectivity in which each point is a vector in $\mathbb{R}^3$ and contains the coordinates of k landmarks, k-ad, selected from the shape. One can determine the equivalence class of each point on this space, that is, the set of points in this space which can be mapped to each other by a certain transformation $\mathbf{G}$. This yields a non-linear Riemannian space $\mathbf{M}$, *shape space*, which is the quotient space of the space $\mathbf{N}$ by the action of the transformation $\mathbf{G}$, i.e. $\mathbf{M} = \mathbf{N}/\mathbf{G}$. For example, the centered and scaled shapes in the k-ad space construct a preshape space S_{km} in which the points can be mapped to each other by the orthogonal group $SO(m)$, i.e. rotation. Thus, shape space is a quotient space, that's, $\sigma_{km} = S_{km}/SO(m)$ [6].

In general, the choice of transformation depends on the geometric property to which the shapes are invariant. The invariance properties can be integrated either into shape space design such that the shape representation is independent of some properties, or into metrics which do not consider certain transformations [16]. In this paper, we pursue the first approach by introducing two shape descriptors which can capture the geometrical differences between healthy and myopathic left ventricle deformations. Our shape space is constructed and equipped with a novel metric in order to measure the distance, therefore, facilitating statistical analysis in shape space to model the shape variability during given deformations. We compare shape deformations by modeling the variability of the intermediate poses over the course of deformation, and compare the spread of these populations in shape space. In general, the means and variations (extrinsic or intrinsic) are adequate for classification in most practical problems [4]. As shape space is a non-linear space, the linear statistical analysis does not induce well-defined shape variabilities [35]. However, we can employ the Exp and Log maps to project each point from non-linear shape space onto linear tangent plane, and estimate the variability on a tangent space as in the Euclidean space using Exponential maps.

2.1 The Exponential Map

Let $\mathbf{M}$ be a complete Riemannian manifold. According to Corollary 1, there exists a geodesic between each pair of points on $\mathbf{M}$. Let $v \in T_p\mathbf{M}$ be a tangent vector, thus there exists a unique geodesic $\gamma_v(t)$, where $\gamma_v(0) = p$ and $\gamma_v'(0) = v$. The *exponential map* $Exp_p(v) : T_p\mathbf{M} \to \gamma_v(t)$ maps the vector v to a point on the geodesic $\gamma_v(t)$. The exponential map preserves the distance from the initial point p, *i.e.*, $d(p, Exp_p(v)) = \|v\|$. Its inverse on the Riemannian manifold is called Log map, Log_x. Let $p, q \in \mathbf{M}$ be two points in a neighborhood on $\mathbf{M}$, then the geodesic between p and q is $d(p, q) = \|Log_p(q)\|$.

2.2 The Exponential map on S^2

For the sphere S^2 with the base of $\mathbf{p} = (0, 0, 1)$, the Exponential map on S^2 is,

$$Exp_{\mathbf{p}}(v) = \left(v_1 \cdot \frac{\sin\|v\|}{\|v\|}, v_2 \cdot \frac{\sin\|v\|}{\|v\|}, \cos\|v\| \right), \quad (1)$$

where $v = (v_1, v_2, 0) \in T_{\mathbf{p}}S^2$ is a tangent vector in the plane x-y (Fig. 1). Inversely, the Log map the point $\mathbf{x} = (x_1, x_2, x_3) \in S^2$ on the tangent plane $T_{\mathbf{p}}S^2$ is,

$$Log_{\mathbf{p}}(x) = \left(x_1 \cdot \frac{\theta}{\sin(\theta)}, x_2 \cdot \frac{\theta}{\sin(\theta)} \right), \quad (2)$$

where $\theta = \arccos(x_3)$ is the spherical distance between the point $\mathbf{p}$ and $\mathbf{x}$. Indeed, S^2 is a symmetric space, and according to Corollary 1, S^2 is a complete space; therefore, every two points can be connected to each other by a geodesic, which is the great circle passing through $\mathbf{p}$.

2.3 Lie Group

The intrinsic analysis on $\mathbf{M}$ makes use of the natural choice of the geodesic distance, in contrast with extrinsic analysis which maps $\mathbf{M}$ into the Euclidean space and computes the distance [17, 6]. The transformations of a smooth manifold can be described by a *Lie group* $\mathbf{G}$, which in turn, is used to compute the geodesic on the Riemannian symmetric spaces [23].

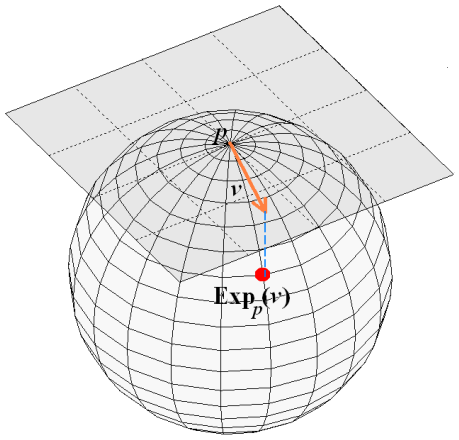

Fig. 1. The exponential map of the tangent vector v on the sphere S^2.

Definition: A Lie group is a group $\mathbf{G}$ that is a smooth manifold in which the multiplication (μ) and inversion (i) maps are smooth, i.e.,

$$\mu : \mathbf{G} \times \mathbf{G} \to \mathbf{G}, (g, h) \to gh \quad (3)$$

$$i : \mathbf{G} \to \mathbf{G}, g \to g^{-1} \quad (4)$$

where $\{g, h\} \in \mathbf{G}$.

Corollary 1: Every symmetric space is geodesically complete, *i.e.*, any two points in the same path component of the space can be connected by a geodesic [19].

Rotations, and affine transformations are some Lie groups acting on the symmetric spaces such as Euclidean space, $\mathbb{R}^n$, and spheres, S^n.

3 The Medial Surface Shape Space and Its Metrics

In this section, we will describe in detail the medial surface shape space and its metrics which can be used to quantify the radial motions of the human heart. The framework can be extended to other motion types as long as there exist shape descriptors which can characterize the particular shape motions.

3.1 Cardiomyopathy

This work aims to classify the normal and abnormal left ventricle (LV) deformations based on the changes in the Wall Thickening (WT) of LV. Cardiomyopathy is the main cardiac disease which affects the wall thickness and its functionality, and is a well-known cause of heart failure or sudden cardiac death in children [25]. In this disease, the normal alignment of muscle cells is disrupted, which obstructs the outflow of blood from the left ventricle. There are three types of Cardiomyopathy (Fig. 2):

- *Dilated CardioMyopathy* (DCM): A portion of the myocardium is dilated, often without any obvious cause. In this condition, the heart becomes weakened and enlarged and cannot pump blood efficiently [12].
- *Hypertrophic CardioMyopathy* (HCM): A portion of the myocardium thickened without any obvious cause [29].
- *Restrictive CardioMyopathy* (RCM): The walls are rigid, and the heart is restricted from stretching and filling with blood properly [24].

In prior research work, the WT is usually computed from the centerline method. In this work, the medial surface is computed, and its features are extracted during one heart cycle for each kind of cardiomyopathy.

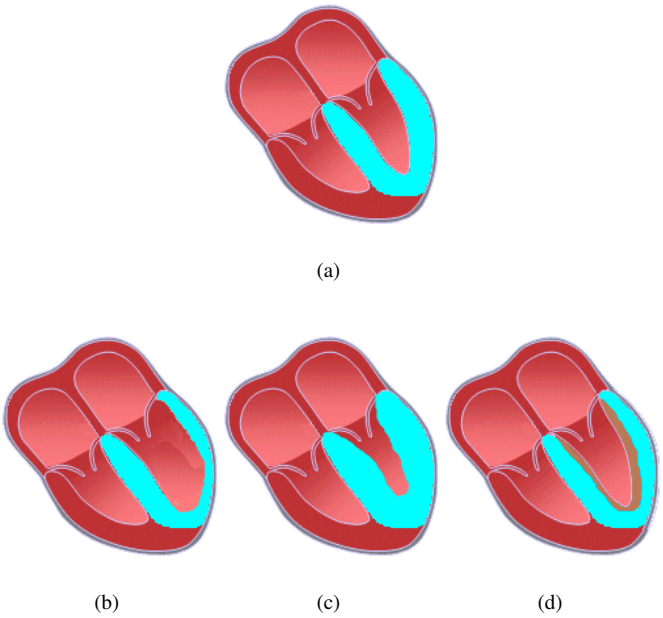

Fig. 2. (a) The diagram of a normal heart with the left ventricle highlighted in blue. The left ventricle with (b) Dilated CardioMyopathy (DCM), (c) Hypertrophic CardioMyopathy (HCM), or (d) Restrictive CardioMyopathy (RCM). The rigid portion of LV with RCM is highlighted in brown.

3.2 Medial Representation

In the medial representation framework, the medial surface ($\mathbf{M}$) consists of some *atoms*. Each atom ($\mathbf{m}$) contains the center of an inscribed sphere ($\mathbf{x}$), the sphere radius (r), and two or three vectors, called *spokes* ($\mathbf{S}_i$), from the sphere centers to the two or three tangent points on the boundary points $\mathbf{y}_i$ (Fig. 3), *i.e.*, $\mathbf{m} = \{\mathbf{x}, r, \mathbf{S}_1, \mathbf{S}_2\} \in \mathbf{M}$. The atoms can be considered as control points on a continuous medial surface [13]. An *end atom* is an atom with three spokes located on the boundary of the medial surface. To simplify the calculations, we do not consider the end atoms in this work.

Let $r(t_1)$ and $r(t_2)$ be the radius elements of an atom $\mathbf{m}$ at two sequential time points t_1 and t_2, respectively. We can estimate the changes of WT at atom $\mathbf{m}$ as $r(t_2)/r(t_1)$, called Proportion of Thick-

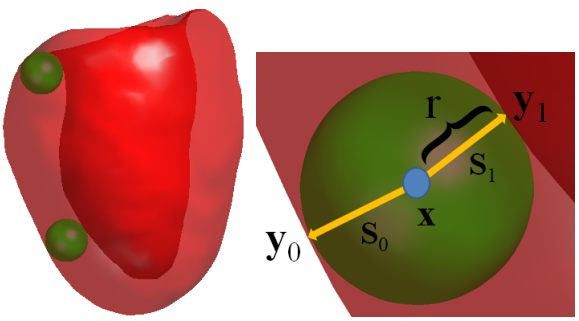

Fig. 3. (a) The LV medial surface contains the centers of inscribed spheres, (b) A non-boundary atom $\mathbf{m}$ contains a position ($\mathbf{x}$), a radius (r), and two spoke directions ($\mathbf{S}_0$, $\mathbf{S}_1$), where its corresponding boundary points $\mathbf{y}_0$ and $\mathbf{y}_1$ can be achieved as, $\mathbf{y}_0 = \mathbf{x} + r\mathbf{S}_0$ and $\mathbf{y}_1 = \mathbf{x} + r\mathbf{S}_1$, respectively.

ness (PT). Since cardiomyopathy affects the myocardium such that the left ventricle cannot contract or expand normally during systolic and diastolic periods of one heart cycle, the changes of wall thickness in myopathic areas are not as healthy areas. Table 1 illustrates the mean and standard deviation of the PT values of the atoms in myopathic and healthy regions of all the subjects. Our observations confirms that PT values of atoms in myopathic regions are close to 1 during one heart cycle, which shows these regions cannot contract or expand as the atoms in healthy subjects whose PT values are < 1 in diastole and > 1 in systole. This makes PT a good candidate to differentiate healthy and myopathic LV's, and localize myopathic regions.

However, due to the existence of noise in the acquired images, as well as the lack of accuracy in the extracted medial surface, *PT* values of some atoms in healthy subjects might also be close to one, which lowers the accuracy of *PT* as a reliable measure. To tackle this problem, two additional measures are introduced, which can correct and enhance the accuracy of *PT*.

3.3 Average of Normal vectors (AoN)

During one heart cycle, the medial surface and wall thickness change according to the left ventricle contraction and expansion. However, in myopathic subjects, one portion of the left ventricle cannot deform consistent with other parts, which in turn affects medial surface and wall thickness. Let $\hat{\mathbf{M}}$ be the set of all atoms whose $PT \approx 1$, $\mathbf{N}$ be normal vector of each atom in $\hat{\mathbf{M}}$, and $\mathbf{N}^{avg}$ be the Average of these Normal vectors (AoN). Fig. 4.a shows the medial surface of a myopathic LV at three sequential time points along with the normal vectors of atoms in $\hat{\mathbf{M}}$. Since the atoms of a myopathic region construct a patch-shape on LV, the direction of AoN does not change noticeably during one heart cycle (Fig. 4.c).

As aforementioned, some atoms of a healthy LV might belong to $\hat{\mathbf{M}}$, *i.e.*, $PT \approx 1$, but since there is no myopathic region on a healthy LV, the $\hat{\mathbf{M}}$ atoms in a healthy LV are distributed all over the medial surface and this distribution might change during one heart cycle at sequential time points (Fig. 4.b). As a result, the direction of AoN changes considerably during one heart cycle, and also during different cycles (Fig. 4.d).

3.4 Mean of Centers (MoC)

Let $\mathbf{x}$ be the center of each atom in $\hat{\mathbf{M}}$ and $\bar{\mathbf{x}}$ be the Mean of the Centers (MoC). In a myopathic LV, the $\hat{\mathbf{M}}$ atoms are concentrated around the myopathic region, thus MoC is close to the medial surface during one heart cycle (Fig. 5.a). In contrast, the $\hat{\mathbf{M}}$ atoms distributed all over the medial surface in a healthy LV, and the corresponding MoC is located inside the medial surface at different time points (Fig. 5.b). Therefore, we can easily calculate MoC of atoms in $\hat{\mathbf{M}}$ and compare its closeness to the medial surface in different subjects to determine abnormalities.

3.5 The Medial Surface Shape Space

In order to quantify and measure the similarity of the LV deformations reflected by $\hat{\mathbf{M}}$, we embed the deforming shapes into a medial surface shape space, where each point corresponds to a certain LV medial surface rather than one atom. Let $\mathbf{L}$ be the medial surface shape space manifold and $\mathbf{l} \in \mathbf{L}$ be a point corresponding to one medial surface. Based on the shape descriptors and characteristics described before,

Table 1. The Mean and Standard Deviation ($Mean \pm SD$) of PT Values in Myopathic and Healthy Regions during Systolic and Diastolic Phases

	Systole (Contraction)	Diastole (Expansion)
Healthy Region	1.38 ± 0.61	0.62 ± 0.31
Myopathic Region	1.12 ± 0.53	0.93 ± 0.42

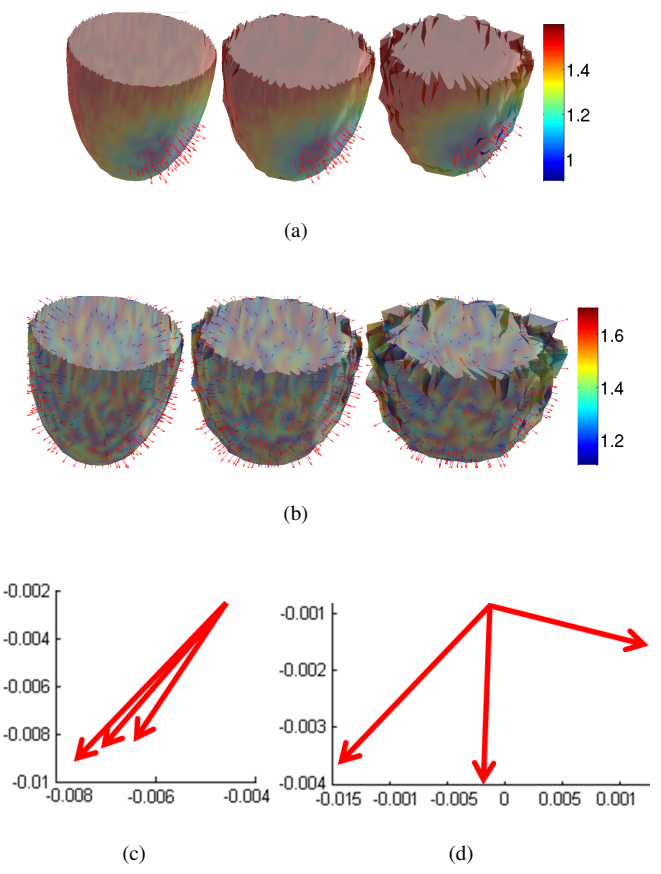

Fig. 4. The medial surface of (a) a myopathic LV and (b) a healthy LV at three time points. Different *PT* values are represented with different colors along with the normal vectors of atoms in $\hat{\mathbf{M}}$. (c) The Average of the Normal vectors (AoN) of the atoms in $\hat{\mathbf{M}}$ have roughly the same direction at three time points in the myopathic LV, but (d) AoN of the atoms in $\hat{\mathbf{M}}$ have considerably different directions in the healthy LV.

we can define the unique shape space as,

$$\mathbf{l} = (\bar{\mathbf{x}}, \hat{r}^{\rho}, \mathbf{N}^{avg}) \in \left\{\mathbb{R}^3 \times \mathbb{R}^+ \times S^2\right\},$$

where $\bar{\mathbf{x}}$ and $\mathbf{N}^{avg}$ are the MoC and AoN of $\hat{\mathbf{M}}$ of $\mathbf{l}$,

$$\hat{r} = \prod_{i \in \hat{\mathbf{M}}} \left(\frac{r_i(t_2)}{r_i(t_1)}\right),$$

is the multiplication of *PT* values over all atoms in $\hat{\mathbf{M}}$, and ρ is a constant measuring the average of the log map distance between the normal vector $\mathbf{N}$ and the corresponding spoke vector $\mathbf{S}$ at all the atoms in $\hat{\mathbf{M}}$. Basically, the introduced shape descriptor uses the normal vectors of the medial surface to confirm the accuracy of *PT* values in different subjects. However, the medial surface as mentioned before contains spokes which are the normal vectors of the boundary, not of the medial surface (Fig. 6).

To take this difference into account, the distance between each spoke and the corresponding normal vector is measured by the log map as in Eq.2,

$$Log_{\mathbf{N}}(\mathbf{S}) = \left(s_1 \cdot \frac{\theta}{\sin(\theta)}, s_2 \cdot \frac{\theta}{\sin(\theta)}\right),$$

where $\mathbf{N}$ is the normal vector of the medial surface, and $\mathbf{S} = (s_1, s_2, s_3)$ is the spoke. The average of log map distance between

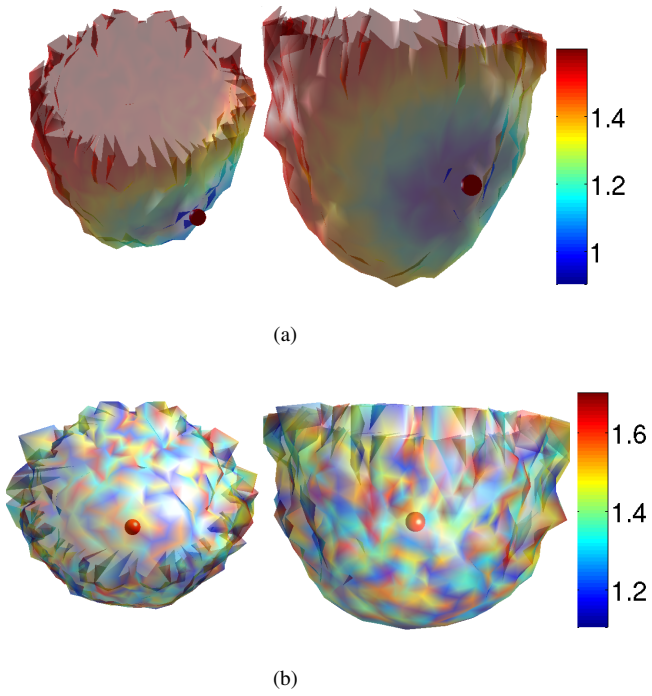

Fig. 5. (a) MoC of a myopathic LV is located in the medial surface, (b) In a healthy LV, the mean is inside the medial surface.

the normal vector $\mathbf{N}$ and the corresponding spoke $\mathbf{S}$ over all the atoms in $\hat{\mathbf{M}}$ is,

$$\rho = \frac{\sum_{\hat{\mathbf{M}}} Log_{\mathbf{N}}(\mathbf{S})}{|\hat{\mathbf{M}}|}.$$

In the following, we prove that the introduced left ventricle medial surface space $\mathbf{L}$ is a diffeomorphic to the quotient space.

Let $\mathbf{L} = \left\{\mathbb{R}^3 \times \mathbb{R}^+ \times S^2\right\}$ be the symmetric space of the medial surfaces, and the group $\mathbf{G} = \left\{\mathbb{R}^3 \times \mathbb{R}^+ \times SO(3)\right\}$ act on it smoothly as,

$$\begin{aligned} \mathbf{G} \times \mathbf{L} \to \mathbf{L} : g \cdot \mathbf{l} &= (\mathbf{v}, s, \mathbf{R}) \cdot (\mathbf{x}, r, \mathbf{S}) \\ &= (\mathbf{x} + \mathbf{t}, r \cdot s, \mathbf{R} \cdot \mathbf{S}). \end{aligned}$$

where $\mathbf{t}$ is the translation, s is the scaling factor, and $\mathbf{R}$ is the rotation matrix. $\mathbb{R}^3$ is a Lie group under vector addition, $\mathbb{R}^+$ is an element

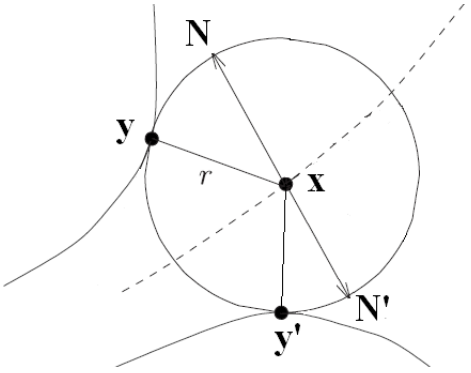

Fig. 6. The extract medial surface contains two spokes which are perpendicular to the boundary at $\mathbf{y}$ and $\mathbf{y}'$, yet the proposed shape descriptor makes use of the normal vectors, $\mathbf{N}$ and $\mathbf{N}'$, of the medial surface.

of the multiplicative Lie group of positive real numbers, and $SO(3)$ is a Lie group under the composition of rotations. Therefore, $\mathbf{G}$ as a product of three Lie groups is also a Lie group [14].

Definition: The *isotropy* subgroup of the base point $\mathbf{b} \in \mathbf{L}$ is the subgroup of $\mathbf{G}$ which leaves $\mathbf{b}$ fixed, *i.e.*, $\mathbf{G_b} = \{g \in \mathbf{G} : g \cdot \mathbf{b} = \mathbf{b}\}$.

Theorem 1: Let $\mathbf{L}$ be a symmetric space and let the isometry group $\mathbf{G}$ act transitively on $\mathbf{L}$. Then the map,

$$\varphi : \mathbf{G}/\mathbf{G}_b \to \mathbf{L},$$

is a diffeomorphism [32].

If $\mathbf{p} = [(0,0,0),(1),p] \in \left\{\mathbb{R}^3 \times \mathbb{R}^+ \times S^2\right\}$ is the base point, where p = (0, 0, 1), then the isotropy subgroup $\mathbf{G_p}$ is,

$$\{(0,0,0) \times (1) \times SO(2)\}.$$

According to Theorem 1, the medial surface space $\mathbf{L}$ is diffeomorphic to the quotient space,

$$\mathbf{G}/\mathbf{G_p} = \left\{\mathbb{R}^3 \times \mathbb{R}^+ \times SO(3)/SO(2)\right\}.$$

3.6 Distance Metric

In our defined medial surface shape space, the geodesic distance connecting two points on the shape space manifold measures the similarity between their corresponding medial surfaces. To measure the distance between two points corresponding to two poses in the space $\mathbf{L}$, we use the log map distance.

Let $\mathbf{l}_1 = (\bar{\mathbf{x}}_1, \hat{r}_1^{\rho}, \mathbf{N}_1^{avg})$ and $\mathbf{l}_2 = (\bar{\mathbf{x}}_2, \hat{r}_2^{\rho}, \mathbf{N}_2^{avg})$ be two LV medial surfaces in $\mathbf{L}$, and $\mathbf{u}_1$ be the tangent vector of $\mathbf{L}$ at point $\mathbf{l}_1$. We project the non-linear shape space onto the linear tangent space using the log map, which preserves the geodesic distance, *i.e.*, $d_g(\mathbf{l}_1, \mathbf{l}_2) = \|Log_{\mathbf{l}_1}(\mathbf{l}_2)\|$, where d_g is the geodesic distance between $\mathbf{l}_1$ and $\mathbf{l}_2$ on the shape space manifold and $Log_{\mathbf{l}_1}(\mathbf{l}_2)$ is their log map. Further, according to the log map definition, $\|Log_{\mathbf{l}_1}(\mathbf{l}_2)\| = \|\mathbf{u}_1\|$; therefore,

$$\|Log_{\mathbf{l}_1}(\mathbf{l}_2)\| = \|\mathbf{u}_1\| = \langle \mathbf{u}_1, \mathbf{u}_1 \rangle^{\frac{1}{2}},$$

which is a Riemannian metric.

Let $g = (\mathbf{v}, s, \mathbf{R})$ be an element of the group $\mathbf{G}$ of isometries acting on $\mathbf{L}$, where $\mathbf{v}$ is the translation vector, s is the scaling factor, and $\mathbf{R}$ is the rotation matrix; therefore, it acts on $\mathbf{l}_1$ as,

$$g \cdot \mathbf{l}_1 = (\mathbf{v} + \bar{\mathbf{x}}_1, s \cdot \hat{r}_1^{\rho}, \mathbf{R} \cdot \mathbf{N}_1^{avg}),$$

since g belongs to the group of isometries,

$$d(\mathbf{l}_1, \mathbf{l}_2) = d(g \cdot \mathbf{l}_1, g \cdot \mathbf{l}_2).$$

In addition, let $\mathbf{p} = [(0,0,0),(1),p_0] \in \left\{\mathbb{R}^3 \times \mathbb{R}^+ \times S^2\right\}$ be the base point, where $p_0 = (0,0,1)$, and $\bar{g} \in \mathbf{G}$ maps $\mathbf{l}_1$ to $\mathbf{p}$, *i.e.*, $\mathbf{p} = \bar{g} \cdot \mathbf{l}_1$, since $\bar{g}$ is an isometry, $d(\mathbf{l}_1, \mathbf{l}_2) = d(\bar{g} \cdot \mathbf{l}_1, \bar{g} \cdot \mathbf{l}_2) = d(\mathbf{p}, \bar{g} \cdot \mathbf{l}_2)$, and

$$\bar{g} \cdot \mathbf{l}_2 = (\bar{\mathbf{x}}_2 - \bar{\mathbf{x}}_1, \frac{\hat{r}_2^{\rho}}{\hat{r}_1^{\rho}}, \mathbf{T} \cdot \mathbf{N}_2^{avg}),$$

where $\mathbf{T}$ is a rotation matrix, such that $\mathbf{T} \cdot \mathbf{N}_1^{avg} = p_0$.

Now, we define the Exponential and Log maps of the LV medial surface shape space as follows,

$$Exp_{\mathbf{p}}(\bar{g} \cdot \mathbf{l}_2) = (\bar{\mathbf{x}}_2 - \bar{\mathbf{x}}_1, exp(\frac{\hat{r}_2^{\rho}}{\hat{r}_1^{\rho}}), Exp_{\mathbf{p}}(\mathbf{T} \cdot \mathbf{N}_2^{avg})), \quad (5)$$

where, $\exp(.)$ is a regular exponential function and $Exp_{\mathbf{p}}(\mathbf{T} \cdot \mathbf{N}_2^{avg})$ is the spherical exponential map (Eq.1), and

$$Log_{\mathbf{p}}(\bar{g} \cdot \mathbf{l}_2) = (\bar{\mathbf{x}}_2 - \bar{\mathbf{x}}_1, log(\frac{\hat{r}_2^{\rho}}{\hat{r}_1^{\rho}}), Log_{\mathbf{p}}(\mathbf{T} \cdot \mathbf{N}_2^{avg})), \quad (6)$$

where, $\log(.)$ is a regular log function and $Log_{\mathbf{p}}(\mathbf{T} \cdot \mathbf{N}_2^{avg})$ is the spherical exponential map (Eq.2).

Based on the defined Log map on the LV shape space, we can define the intended shape space metric. Since the log map projects the points on the linear tangent plane, the magnitude of the log map is defined using the linear Euclidean distance measure as,

$$\begin{aligned} d(\mathbf{p}, \bar{g}\cdot\mathbf{l}_2) &= \|Log_{\mathbf{p}}(\bar{g}\cdot\mathbf{l}_2)\| \\ &= \left[\|\bar{\mathbf{x}}_2 - \bar{\mathbf{x}}_1\|^2 + \|\rho_2\cdot log(\hat{r}_2) - \rho_1\cdot log(\hat{r}_1)\|^2 \right. \\ &\quad \left. + \|Log_{\mathbf{p}}(\mathbf{T}\cdot\mathbf{N}_2^{avg})\|^2\right]^{\frac{1}{2}}, \end{aligned} \tag{7}$$

in which, $\|Log_{\mathbf{p}}(\mathbf{T}\cdot\mathbf{N}_2^{avg})\| = \left\|Log_{\mathbf{N}_1^{avg}}(\mathbf{N}_2^{avg})\right\|$, which is the spherical log map between $\mathbf{N}_1^{avg}$ and $\mathbf{N}_2^{avg}$. As $d(\mathbf{l}_1,\mathbf{l}_2) = d(\mathbf{p}, \bar{g}\cdot\mathbf{l}_2)$; therefore,

$$\begin{aligned} d(\mathbf{l}_1,\mathbf{l}_2) &= \|Log_{\mathbf{l}_1}(\mathbf{l}_2)\| \\ &= \left[\|\bar{\mathbf{x}}_2 - \bar{\mathbf{x}}_1\|^2 + \|log(\hat{r}_2^{\rho_2}) - log(\hat{r}_1^{\rho_1})\|^2 \right. \\ &\quad \left. + \left\|Log_{\mathbf{N}_1^{avg}}(\mathbf{N}_2^{avg})\right\|^2\right]^{\frac{1}{2}}. \end{aligned} \tag{8}$$

3.7 Deformation Classification

Let $\mathbf{l}_1, ..., \mathbf{l}_n \in \mathbf{L}$ be n points in shape space corresponding to n poses of the LV during one heart cycle. As mentioned in Section 3.3 and Section 3.4, the variations of AoN and MoC of a myopathic LV is smaller than those of a healthy LV. As a result, the points $\mathbf{l}_i$ are closer to each other in a myopathic LV than in a healthy LV. Therefore, the variance of the points which reveals the closeness of the points $\mathbf{l}_i$, can be used to classify healthy and myopathic LV's.

Since the points $\mathbf{l}_i$'s are located on a non-linear shape space manifold, we calculate the *intrinsic variance* of $\mathbf{l}_i$'s for each LV rather than the ordinary variance. First, the *intrinsic mean* of the points $\mathbf{l}_i$'s is computed based on the proposed metric as following [13],

Algorithm 1 *Intrinsic Mean*

Require: $\mathbf{l}_1, ..., \mathbf{l}_n \in \mathbf{L}$
Ensure: $\mu \in \mathbf{L}$
1: $\mu_0 = \mathbf{l}_1$
2: **repeat**
3: $\quad \Delta\mu = \frac{1}{n}\cdot\Sigma_{i=1}^{n} d_g(\mu_j, \mathbf{l}_i) = \frac{1}{n}\cdot\Sigma_{i=1}^{n}\left\|Log_{\mu_j}(\mathbf{l}_i)\right\|$
4: $\quad \mu_{j+1} = Exp_{\mu_j}(\Delta\mu)$
5: **until** $\|\Delta\mu\| > \epsilon$

where $Exp_{\mu_j}(\Delta\mu)$ is the exponential map (Eq.5), determining the changes of the intrinsic mean on the shape space manifold, and ϵ is the convergence threshold.

Next, the intrinsic variance σ^2 is calculated as,

$$\sigma^2 = \frac{1}{n-1}\cdot\Sigma_{i=1}^{n} d_g^2(\mu, \mathbf{l}_i) = \frac{1}{n-1}\cdot\Sigma_{i=1}^{n}\|Log_{\mu}(\mathbf{l}_i)\|^2,$$

where μ is the intrinsic mean of $\mathbf{l}_i$'s, and $\|Log_{\mu}(\mathbf{l}_i)\|$ is the geodesic distance between μ and $\mathbf{l}_i$ based on the proposed metric.

4 Experimental Results on Synthetic Data

Some genus zero surfaces with one boundary are generated to simulate the LV medial surface and the wall thickness is simulated as a function on the surfaces. Then, the surfaces and their thickness functions are changed in accordance with the LV deformation. As the point correspondences are known, there is no need for the surface registration. The end atoms located on the boundary cause instability in the analysis, thus we avoid such instability by removing all the end atoms.

After calculation of AoN and MoC values, the location of each intermediate pose is determined in shape space; and then, the intrinsic variance of the corresponding points of each deformation is computed accordingly. The synthetic datasets simulating myopathic LV's show noticeably less variances than the other datasets.

Table 2. Performance of the Algorithm Against Noisy Datasets with Different Percentages of Additive Noise Variance

Variance of Medial Surface Noise	Uniform Noise	Gaussian Noise
1%	97.3%	96.5%
2.5%	94.9%	93.8%
5%	91.6%	90.1%
Variance of Wall Thickness Noise	**Uniform Noise**	**Gaussian Noise**
1%	98.1%	97.4%
2.5%	96.8%	95.2%
5%	92.2%	90.3%

4.1 Noise Resistance

Due to inaccuracy in the medial surface extraction and also due to existence of noise in the acquired images, the medial surface may not be extract accurately. To evaluate the performance of the method against these inaccuracies, some uniform and Gaussian noises are added to the medial surface at the first step. Table 2 shows the percentage of misclassified deformations with different noise distributions. The performance is robust to the additive noise.

Furthermore, the inaccuracy in the extracted medial surface incurs the inaccurate wall thickness. Thus, some noises are added to the 2D thickness function under the condition that the error does not overwhelm the motion characteristics. As shown in Table 2, this method is also resistance against inaccurate wall thickness.

4.2 Myopathic Region Size

Measuring the myopathic region size can reveal the severity of the disease. Towards this end, some 2D functions simulating different sizes of the myopathic regions are generated as the thickness functions along with some additive noises (Fig. 7). As the myopathic region size can reveal the severity of the disease, some 2D functions simulating different sizes of the myopathic regions were generated as the thickness functions, and contaminated with some additive noises. Table 3 illustrates the mean and standard deviation of the spherical log map distance between AoN vectors at different time points in each dataset, and the normalized distance between MoC and the center of the medial surface, i.e. the average of all the atoms in the medial surface, in all the datasets with various myopathic region sizes. The experiments reveal that as the myopathic region grows, its MoC moves towards inside the medial surface, yet its AoN vectors at different time points are still coherent. On the contrary, as the myopathic region becomes smaller, its AoN vectors become more diverged, yet its MoC is still on the medial surface. This means that the method is capable to detect myopathic regions of different sizes. Especially, the capability of detecting tiny myopathic regions can lead to the early diagnosis.

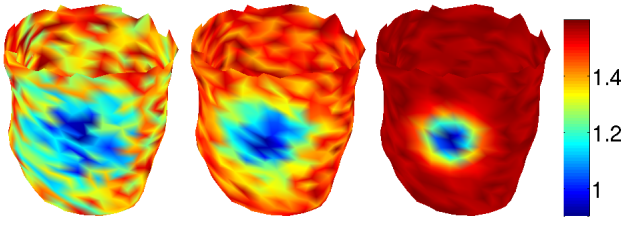

Fig. 7. The medial surface classification is affected by the abnormality size. If the abnormality is large (Left), MoC of the patch is inside the surface; on contrary, if it is small (Right), AoN might diverge away from each other.

Table 3. The Changes of AoN and MoC for Different Myopathic Sizes, C1: The Proportion of the Myopathic Region to the Total Medial Surface, C2: The Mean and Standard Deviation of the Spherical Log Map Distance Between AoN Vectors at Sequential Time Points, C3: The Normalized Distance Between MoC and the Center of the Medial Surface at Sequential Time Points

C1	C2	C3
10%	0.32 ± 0.27	0.95 ± 0.04
20%	0.21 ± 0.20	0.88 ± 0.07
40%	0.15 ± 0.17	0.81 ± 0.11

5 Experimental Results on Real Imaging Data

The CT and gated images of the left ventricle during one heart cycle were acquired from 19 control subjects and 25 myopathic subjects whose cardiac abnormalities were verified by cardiologists. Each dataset contains eight time points during one heart cycle. First, the medial surfaces of sequential poses were extracted with 400 atoms at each pose using the method in [33] as follows,

1. An initial left ventricle segmented from the CT images is used as template.
2. We use qhull (www.qhull.org) to compute the Voronoi Skeleton of the segmented template and prune the medial surface.
3. We use an extrinsic registration method based on Thin-Plate Splines (TPS) [30, 43] which uses the intensity information along with some landmarks selected on apex, epicardium and endocardium surfaces, and register the LV to the template.
4. We warp the segmentation image and the medial surface using the deformation field estimated by TPS.

Note that, in our framework, any other non-rigid registration method can be utilized, such as Advanced Normalization Tools (ANTS) [1, 22]. Furthermore, we can use multiple templates and fuse the results of segmentation using the majority voting or STAPLE [38] methods in order to achieve more accurate medial surface. Finally, the location of each pose embedded in the medial surface shape space is calculated along with the intrinsic variance for each subject (Fig. 8).

Fig. 10 shows the automatic classification pipeline along with the automatic processing steps. Table 4 illustrates the sensitivity and specificity of our method using $\sigma^2 = 0.1$. The appropriate threshold was determined by calibration across a retrospective set of myopathic and healthy subjects by drawing the histogram of the intrinsic variances for all the subjects (Fig 9). As seen, $\sigma^2 = 0.1$ can split two healthy and myopathic groups. The method outperforms other methods based on the LV cavity, mean radial displacement and mean radial velocity [28]. In fact, this indicator is very sensitive in detecting myopathic regions.

To better visualize dis/similarity of the deformations, the corresponding medial surface points on the shape space manifold are projected on a 2D plane using the MultiDimensional Scaling method (MDS) [9] and based on the proposed metric. Let $\mathbf{L} = \{\mathbf{l}_1, \ldots, \mathbf{l}_n\}$ be n intermediate medial surface. We define the similarity matrix $\mathbf{D}$, where $d_{i,j} = d(\mathbf{l}_i, \mathbf{l}_j)$ is the similarity between medial surfaces i and j as in Eq 8. We minimize the difference between pair-wise distances in the medial surface shape space, e.g. $d(\mathbf{l}_i, \mathbf{l}_j)$, and the distance between their corresponding points on the 2D space, e.g. $\|\mathbf{x}_i - \mathbf{x}_j\|$, that's,

$$\min_{\mathbf{x}_1,\ldots,\mathbf{x}_n} \sum_{i<j} (\|\mathbf{x}_i - \mathbf{x}_j\| - d_{i,j})^2 \tag{9}$$

For clear illustration, Fig. 11 only shows the points corresponding to two randomly selected myopathic subjects and two randomly selected healthy subjects after projection on the 2D plane. In the myopathic subjects, since MoC's and AoN's do not change in sequential poses, their corresponding embedded points are located close to each other on the shape space manifold, so are their corresponding points on the 2D plane after the MDS projection as shown in Fig. 11. Our prototype comparative visualization and classification system allows domain users to select any of the point in the projected shape space to identify a corresponding pose of the left ventricle of the human subject. For a cardiomyopathic human subject, the myopathic region can be automatically localized and visualized. The system is a stone alone program. The input data was the standard format of DICOM (Digital Imaging and Communications in Medicine) which is a standard for storing and transmitting information in medical imaging. After segmentation and normalization of the left ventricle, the medial surface was extracted, and the suspicious myopathic areas were calculated using our approach and marked on the 3D left ventricle surface using VTK(Visualization Toolkit) libraries. Three junior and two senior cardiologists from our institution have evaluated our system, each tested $4 \sim 5$ normal and 5 abnormal subjects. After loading the DICOM images, the cardiologists navigate through the DICOM slices and visually inspect the wall thickness in the left ventricle which usually take $10 \sim 20$min for each subject, and investigate the location of myopathic region, and then, compare it with our results for efficacy test. The prototype system has been commended by all five cardiologists, who have tested it, for its ease of use, accuracy of classification and clear visualization in the diagnosis of cardiomyopathy.

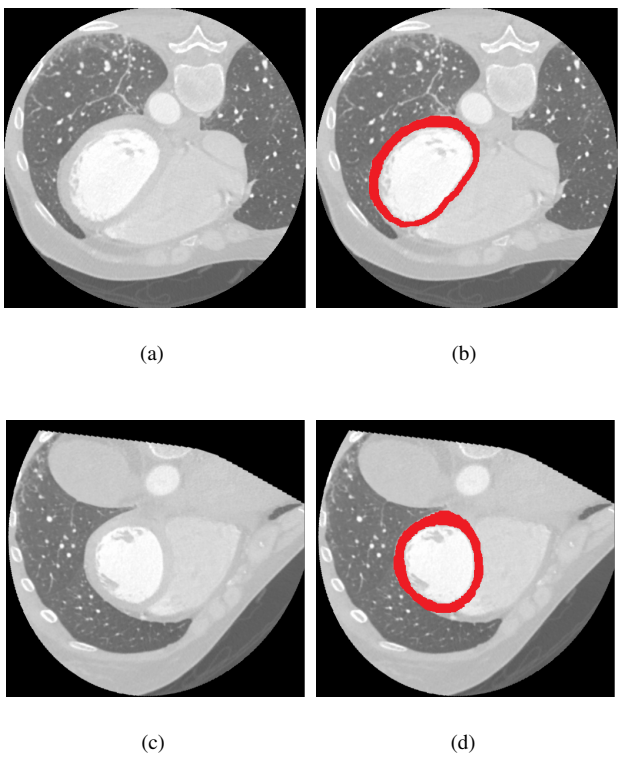

(a) (b) (c) (d)

Fig. 8. The left ventricle from (a) the axial view, and (c) the short axis view. As highlighted in (b) and (d), the left ventricle can be easily segmented from low intensity air in lungs and the high intensity contrast agent inside.

Table 4. Sensitivity and Specificity of the Proposed Method for $\sigma^2 = 0.1$

	Sensitivity	Specificity
Our Proposed Method	92.0%	89.5%
Mean Systolic Radial	79.4%	54.9%
Mean Radial Displacement	76.2%	70.9%

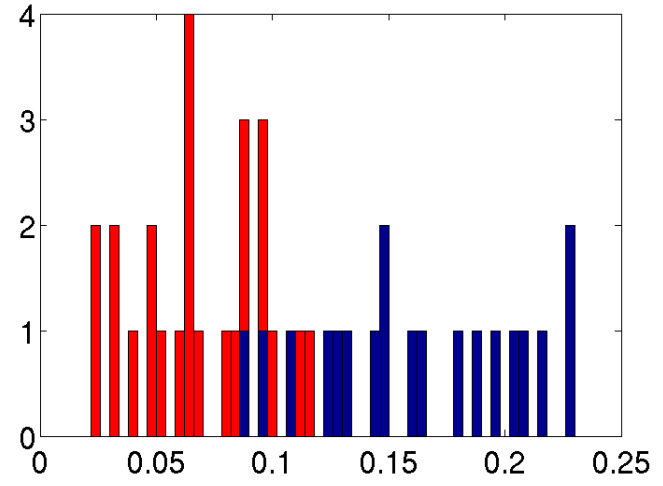

Fig. 9. The histogram of the intrinsic variances for all the subjects where the blue bins illustrate the variances of the healthy subjects, whereas the red bins show those of the myopathic subjects.

6 Conclusions

This paper has presented a novel comparative visualization and classification method based on medial surface shape space, which can quantify shape motions and localize the inconsistently deforming regions across subjects. In order to determine the similarity between two medial representations, we introduce a new metric which measures the geodesic distance between two points corresponding to two medial representations on the shape space manifold. This metric reconciles to the non-linearity of the shape motion path on shape space.

We have applied to the classification and comparison of the left ventricle motions. In particular, we have employed *PT* values of each LV to detect the candidate myopathic locations. To improve the performance of the *PT* values, two additional novel shape descriptors, AoN and MoC, are introduced to capture the non-linearity of the LV deformation for diagnosis of the cardiomyopathy disease. Our experiments have shown that it is of great use to diagnose the myopathic left ventricles in which myopathic regions do not work normally and the wall thickness during heart motion is affected accordingly. The experimental results show that this method can automatically classify the healthy and myopathic subjects as well as detect myopathic regions on the left ventricle well. This method shows remarkable sensitivity and specificity, which outperforms other conventional cardiac diagnostic methods.

The choice of number atoms to capture the deformation of the left ventricle might lead to incorrect sampling. Sun *et al.* [33] employ around 200 atoms, whereas we use 400 atoms for the medial surface extraction which has more sensitivity. However, we can use a multi-resolution framework to extract a low-resolution medial surface in the coarsest resolution, increase the sampling in the areas which are more likely to be myopathic, i.e. the areas with PT values close to 1, and then, investigate their spatial distribution from coarsest to finest resolution. This issue will be investigated further in the future work.

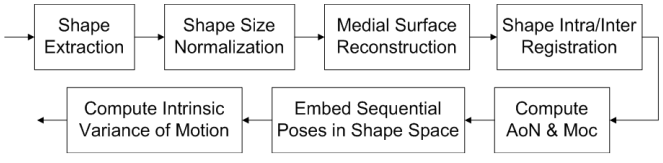

Fig. 10. The motion image processing and classification pipeline.

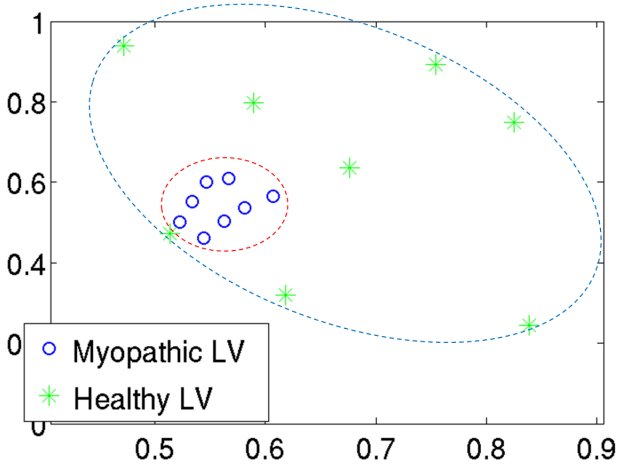

(a)

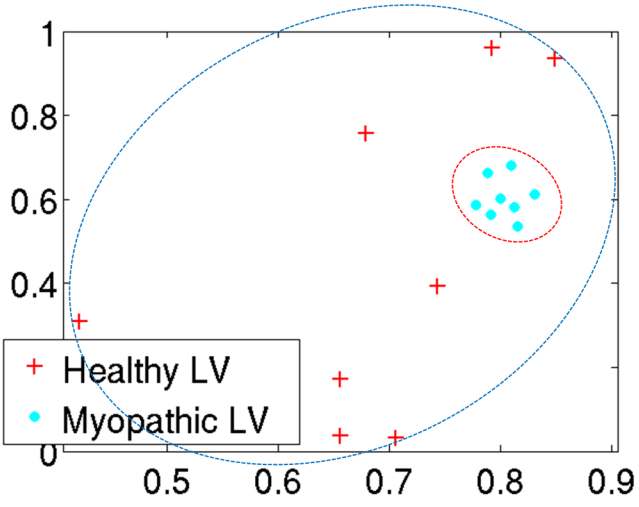

(b)

Fig. 11. The projection of two healthy and two myopathic LV motions (each containing 8 motion snapshots) onto the 2D plane illustrates that the points corresponding to the healthy LV are scattered all over the 2D plane, but those of the myopathic LV are concentrated on the same part of the 2D plane.

Acknowledgments

We would like to thank the reviewers for their valuable comments. This work is supported in part by the research grants, including the National Science Foundation grants IIS-0915933, IIS-0937586, and IIS-0713315, as well as the National Institute of Health grants 1R01NS058802-01A2 and 2R01NS041922-05A1.

References

[1] B. B. Avants, C. L. Epstein, M. Grossman, and J. C. Gee. Symmetric diffeomorphic image registration with cross-correlation: Evaluating automated labeling of elderly and neurodegenerative brain. *Medical image analysis*, 12(1):26–41, 2008.

[2] H. Azhari, S. Sideman, J. L. Weiss, E. P. Shapiro, M. L. Weisfeldt, W. L. Graves, W. J. Rogers, and R. Beyar. Three-dimensional mapping of acute ischemic regions using mri: wall thickening versus motion anal-

ysis. *American Journal of Physiology-Heart and Circulatory Physiology*, 259(5):H1492–H1503, 1990.

[3] L. Bartram and C. Ware. Filtering and brushing with motion. *Information Visualization*, 1(1):66–79, 2002.

[4] A. Bhattacharya. *Nonparametric statistics on manifolds with applications to shape spaces*. ProQuest, 2008.

[5] R. Bhattacharya and A. Bhattacharya. Statistics on manifolds with applications to shape spaces. *Perspectives in Mathematical Sciences. Indian Statistical Institute, Bangalore*, 2008.

[6] R. Bhattacharya and V. Patrangenaru. Large sample theory of intrinsic and extrinsic sample means on manifolds: Ii. *Annals of statistics*, pages 1225–1259, 2005.

[7] E. Bolson and F. Sheehan. Centersurface model for 3d analysis of regional left ventricular function. In *Proceedings of Computers in Cardiology Conference*, pages 735–738, 1993.

[8] J. Corney, H. Rea, D. Clark, J. Pritchard, M. Breaks, and R. MacLeod. Coarse filters for shape matching. *IEEE Computer Graphics and Applications*, 22(3):65–74, 2002.

[9] T. Cox and M. Cox. *Multidimensional scaling*, volume 1. CRC Press, 2001.

[10] J. Damon. Smoothness and geometry of boundaries associated to skeletal structures i: Sufficient conditions for smoothness. In *Annales de l'institut Fourier*, volume 53, page 1941. Chartres: L'Institut, 1950-, 2003.

[11] N. Elmqvist and P. Tsigas. Causality visualization using animated growing polygons. In *IEEE Symposium on Information Visualization*, pages 189–196, 2003.

[12] A. S. Fauci et al. *Harrison's principles of internal medicine*, volume 2. McGraw-Hill Medical New York, 2008.

[13] P. Fletcher, S. Pizer, and S. Joshi. Shape variation of medial axis representations via principal geodesic analysis on symmetric spaces. *Statistics and Analysis of Shapes*, pages 29–59, 2006.

[14] P. T. Fletcher, S. Joshi, C. Lu, and S. M. Pizer. Gaussian distributions on lie groups and their application to statistical shape analysis. In *Information Processing in Medical Imaging*, pages 450–462. Springer, 2003.

[15] A. F. Frangi, W. J. Niessen, and M. A. Viergever. Three-dimensional modeling for functional analysis of cardiac images, a review. *IEEE Transactions on Medical Imaging*, 20(1):2–5, 2001.

[16] M. Fuchs, B. Jüttler, O. Scherzer, and H. Yang. Shape metrics based on elastic deformations. *Journal of Mathematical Imaging and Vision*, 35(1):86–102, 2009.

[17] H. Hendriks and Z. Landsman. Mean location and sample mean location on manifolds: Asymptotics, tests, confidence regions. *Journal of Multivariate Analysis*, 67(2):227–243, 1998.

[18] G. Ji and H.-W. Shen. Dynamic view selection for time-varying volumes. *IEEE Transactions on Visualization and Computer Graphics*, 12(5):1109–1116, 2006.

[19] J. Jost. *Universitext: Riemannian Geometry and Geometric Analysis*. Springerverlag Berlin Heidelberg, 2011.

[20] D. Kendall. The diffusion of shape. *Advances in Applied Probability*, 9(3):428–430, 1977.

[21] D. G. Kendall. Shape manifolds, procrustean metrics, and complex projective spaces. *Bulletin of the London Mathematical Society*, 16(2):81–121, 1984.

[22] A. Klein, J. Andersson, B. A. Ardekani, J. Ashburner, B. Avants, M.-C. Chiang, G. E. Christensen, D. L. Collins, J. Gee, P. Hellier, et al. Evaluation of 14 nonlinear deformation algorithms applied to human brain mri registration. *Neuroimage*, 46(3):786–802, 2009.

[23] H. Krim and A. Yezzi Jr. *STATISTICS AND ANALYSIS OF SHAPE*. Springer, 2007.

[24] S. S. Kushwaha, J. T. Fallon, and V. Fuster. Restrictive cardiomyopathy. *New England Journal of Medicine*, 336(4):267–276, 1997.

[25] B. Maron et al. Cardiovascular preparticipation screening of competitive athletes: a statement for health professionals from the sudden death committee (clinical cardiology) and congenital cardiac defects committee (cardiovascular disease in the young), american heart association. *Circulation*, 94(4):850–856, 1996.

[26] A. V. Moere. Time-varying data visualization using information flocking boids. In *IEEE Symposium on Information Visualization*, pages 97–104, 2004.

[27] S. M. Pizer, K. Siddiqi, G. Székely, J. N. Damon, and S. W. Zucker. Multiscale medial loci and their properties. *International Journal of Computer Vision*, 55(2-3):155–179, 2003.

[28] M. Qazi, G. Fung, S. Krishnan, J. Bi, R. Bharat Rao, and A. Katz. Automated heart abnormality detection using sparse linear classifiers. *IEEE Engineering in Medicine and Biology Magazine*, 26(2):56–63, 2007.

[29] P. Richardson, R. McKenna, M. Bristow, B. Maisch, B. Mautner, J. O'connell, E. Olsen, G. Thiene, J. Goodwin, I. Gyarfas, et al. Report of the 1995 world health organization/international society and federation of cardiology task force on the definition and classification of car diomyopathies. *Circulation*, 93(5):841–842, 1996.

[30] K. Rohr, H. Stiehl, R. Sprengel, T. Buzug, J. Weese, and M. Kuhn. Landmark-based elastic registration using approximating thin-plate splines. *IEEE Transactions on Medical Imaging*, 20(6):526–534, 2001.

[31] F. H. Sheehan, E. L. Bolson, H. T. Dodge, D. G. Mathey, J. Schofer, and H. Woo. Advantages and applications of the centerline method for characterizing regional ventricular function. *Circulation*, 74(2):293–305, 1986.

[32] P. Sjogren. *Riemannska Symmetriska Rum*. Matematiska Institutionen, Chalmers Tekniska Hogskola och Goteborgs Universitet, 1987.

[33] H. Sun, B. Avants, A. Frangi, F. Sukno, J. Gee, and P. Yushkevich. Cardiac medial modeling and time-course heart wall thickness analysis. *Proceedings of International Conference on Medical Image Computing and Computer-Assisted Intervention*, pages 766–773, 2008.

[34] H. Sun, B. B. Avants, A. F. Frangi, S. Ordas, J. C. Gee, and P. A. Yushkevich. Branching medial models for cardiac shape representation. In *Proceedings of the 5th IEEE International Symposium on Biomedical Imaging: From Nano to Macro*, pages 1485–1488, 2008.

[35] A. Swann and N. H. Olsen. Linear transformation groups and shape space. *Journal of Mathematical Imaging and Vision*, 19(1):49–62, 2003.

[36] T. B. Terriberry, G. Gerig, et al. A continuous 3-d medial shape model with branching. In *1st MICCAI Workshop on Mathematical Foundations of Computational Anatomy: Geometrical, Statistical and Registration Methods for Modeling Biological Shape Variability*, pages 80–89, 2006.

[37] C. Ware, E. Neufeld, and L. Bartram. Visualizing causal relations. In *Proceedings of IEEE Information Visualization*, volume 99, 1999.

[38] S. K. Warfield, K. H. Zou, and W. M. Wells. Simultaneous truth and performance level estimation (staple): an algorithm for the validation of image segmentation. *IEEE Transactions on Medical Imaging*, 23(7):903–921, 2004.

[39] P. Yushkevich. Continuous medial representation of brain structures using the biharmonic PDE. *NeuroImage*, 45(1):S99–S110, 2009.

[40] P. A. Yushkevich, H. Zhang, and J. C. Gee. Continuous medial representation for anatomical structures. *IEEE Transactions on Medical Imaging*, 25(12):1547–1564, 2006.

[41] C. Zhang and T. Chen. Efficient feature extraction for 2d/3d objects in mesh representation. In *Proceedings of International Conference on Image Processing*, volume 3, pages 935–938, 2001.

[42] G. Zou, J. Hua, Z. Lai, X. Gu, and M. Dong. Intrinsic geometric scale space by shape diffusion. *IEEE Transactions on Visualization and Computer Graphics*, 15(6):1193–1200, 2009.

[43] G. Zou, J. Hua, and O. Muzik. Non-rigid surface registration using spherical thinplate splines. In *Proceedings of International Conference on Medical Image Computing and Computer-Assisted Intervention*, volume 4791, pages 367–374, 2007.